Journal of the Korean Physical Society
https://doi.org/10.1007/s40042-021-00391-w

Online ISSN 1976-8524
Print ISSN 0374-4884

REVIEW - FLUIDS, PLASMA AND PHENOMENOLOGY

Review of laser-plasma physics research and applications in Korea

W. Bang[1] · B. I. Cho[1] · M. H. Cho[2] · M. S. Cho[1] · M. Chung[3] · M. S. Hur[3] · G. Kang[1] · K. Kang[1] · T. Kang[3] · C. Kim[2] · H. N. Kim[4] · J. Kim[5] · K. B. Kim[6] · K. N. Kim[4,8] · M. Kim[1] · M. S. Kim[2] · M. Kumar[3] · H. Lee[1] · H. W. Lee[7] · K. Lee[4] · I. Nam[2] · S. H. Park[7] · V. Phung[1] · W. J. Ryu[4] · S. Y. Shin[7] · H. S. Song[3] · J. Song[1] · J. Won[1] · H. Suk[1]

Received: 31 August 2021 / Revised: 4 October 2021 / Accepted: 27 October 2021

Abstract

Laser plasmas can be produced when high-power laser beams are focused in matter. A focused laser beam of TW(terawatt)-level high power has an extremely strong electric field, so neutral atoms are immediately ionized by the laser electric field, leading to a laser-produced plasma. The laser plasma can be produced by small table-top TW lasers based on the CPA (chirped-pulse amplification) technique, and now they are rather easily available even in university laboratories. In Korea, there are several CPA-based TW (or even petawatt) lasers in a few institutions, and they have been used for diverse laser plasma physics research and applications, including the laser acceleration for electrons and ions, high-power THz (tera-hertz) generation, advanced light sources, high-energy-density plasmas, plasma optics, etc. This paper reviews some of the laser plasma physics research and applications that have been performed in several universities and research institutes.

Keywords Basic laser-plasma physics · Laser plasma accelerator · Radiation source · High-energy-density plasma · Plasma optics

1 Introduction

Laser-plasmas can be produced if a high peak power laser pulse is focused in matter. This can be realized if a TW-level laser beam is focused to a small spot size, for example, 10 μm in radius, leading to an intensity of $I > 10^{17}$ W/cm^2. In this situation, atoms in the matter are ionized by the strong electric field of the laser beam given by $E_0 = \left(2I/\varepsilon_0 c\right)^{1/2}$, where ε_0 and c are the electric permittivity and the light velocity in free space, respectively. According to the BSI (barrier-suppression ionization) model [1], laser intensity of $I = 10^{17}$ W/cm^2 is strong enough to produce even N^{5+} ions if nitrogen atoms are exposed to the laser beam. Hence, the laser plasma research is closely related with the development of high power lasers and it has a rather short history compared with other types of plasma research.

The focused laser intensity has increased sharply since the first working laser (ruby laser) was successfully developed by T. Maiman in 1960. Invention of the Q-switching method increased the laser intensity by orders of magnitude, and the mode-locking method made it possible to develop a short pulse, high peak power laser. The CPA (chirped-pulse amplification) technique [2], which stretches the original laser pulse in time by four orders of magnitude and compresses it again after amplification in energy, led to the development of small table-top terawatt (T^3) lasers, providing a strong momentum for active laser plasma physics research around the world since the 1990s. In recent years, CPA-based lasers reached a record-high focused intensity up to the level of

✉ H. Suk
hysuk@gist.ac.kr

1 Department of Physics and Photon Science, Gwangju Institute of Science and Technology, Gwangju 61005, Korea

2 Pohang Accelerator Laboratory, Pohang 37673, Korea

3 Department of Physics, Ulsan National Institute of Science and Technology, Ulsan 44919, Korea

4 Radiation Center for Ultrafast Science, Korea Atomic Energy Research Institute, Daejeon 34057, Korea

5 Electro-Medical Device Research Center, Korea Electrotechnology Research Institute, Ansan 15588, Korea

6 Department of Radiation Oncology, Korea Institute of Radiological and Medical Sciences, Seoul 01812, Korea

7 Department of Accelerator Science, Korea University Sejong Campus, Sejong 30019, Korea

8 Present Address: Laser Optics Team, HB Technology Co. Ltd, Ansan 31419, Korea

10^{23} W/cm^2 [3]. Figure 1 shows the remarkable progress of the laser intensity up to the nearly relativistic proton regime.

Figure 2 shows that several TW or even PW laser systems have been installed in Korea so far and that they have been used for diverse research and applications. The first TW laser system dates back to 1994. At that time, a 2 TW Nd:glass laser system was developed at KAIST (Korea Advanced Institute of Science and Technology) and it could deliver a laser pulse with an energy of 80 J and a pulse duration of 40 ps at a wavelength of 1.054 μm. In 2002, another 2 TW laser system was installed at KERI (Korea Electrotechnology Research Institute), where the CPA-based Ti:sapphire/Nd:glass hybrid laser system could provide an energy of 1.4 J and a pulse duration of 700 fs [4]. KAERI (Korea Atomic Energy Research Institute) developed a 30 TW Ti:sapphire laser system and KERI had another 20 TW Ti:sapphire laser in 2009. The Department of Physics and Photon Science (DPPS) at GIST (Gwangju Institute of Science and Technology) also developed a 20 TW Ti:sapphire laser system [5]. APRI (Advanced Photonics Research Institute) at GIST developed a 100 TW Ti:sapphire laser system and upgraded it to 1.5 PW [6], and then IBS/APRI/GIST increased the power to 4.2 PW (20 fs in duration) in 2017 [7]. ETRI (Electronics and Telecommunications Research Institute) also installed a 200 TW Ti:sapphire laser system and upgraded it to 500 TW later. All of these high-power lasers have been used for diverse laser plasma physics research and applications, including electron acceleration, ion generation, high-energy–density (HED) plasma physics, THz generation, plasma optics, etc.

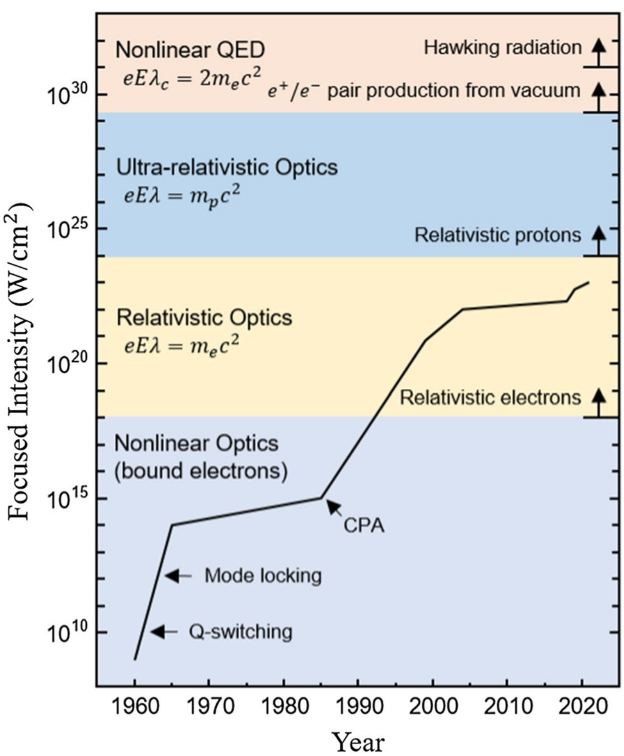

Fig. 1 Evolution of the laser intensity since the invention of a laser, showing remarkable progress up to the nearly relativistic proton regime

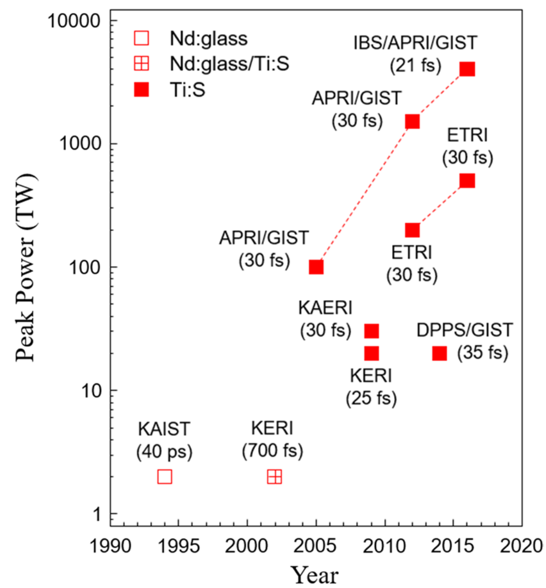

Fig. 2 History of high-power laser systems in Korea, where all TW/PW lasers are still working and are actively used for research except for the first laser

In this paper, we review some laser plasma research activities in several universities and research institutes in Korea, including GIST, PAL, UNIST, KIRAMS, KAERI, KERI, ETRI, and Korea University Sejong Campus. Major activities of IBS/APRI/GIST were reviewed in the separate article [8]; thus, they are not included here. This paper will provide a brief overview of basic laser plasma properties first, and then some research results from those universities and research institutes will be described in subsequent sections.

2 Brief overview of basic laser plasma properties

Laser-produced plasmas have many unique and interesting features [9, 10]. For example, electrons in a plasma experience electric and magnetic forces, $\boldsymbol{F} = e(\boldsymbol{E} + \boldsymbol{v} \times \boldsymbol{B})$, if a laser pulse is applied. The quivering electrons can have relativistic velocities if the focused laser intensity is $I \sim 10^{18}$ W/cm^2. This kind of relativistic phenomenon can be described by using the normalized vector potential given by $a_0 = p/m_0c = eE/m_e\omega_0c$, where p is the electron momentum, m_e the electron rest mass, e the electron charge, and ω_0 is the laser frequency. In practical units, the normalized vector potential is given by $a_0 = 0.85 \times 10^{-9}\sqrt{I[\mathrm{W/cm^2}]}\lambda[\mu\mathrm{m}]$

[9], where λ is the laser wavelength. Thus, $a_0 = p/m_e c \sim 1$ implies that the plasma electrons move relativistically, which can be achieved if the laser intensity is $I > 10^{18}$ W/cm^2 for $\lambda = 0.8$ μm (Ti:sapphire laser wavelength). If the laser intensity is $I > 10^{24}$ W/cm^2, even protons can have relativistic velocities. This kind of relativistic plasma can provide a self-focusing effect for an intense laser beam propagating in the plasma as the index of refraction of the plasma is given by $\eta = \left[1 - \left(\omega_p/\omega_0\right)^2\right]^{1/2}$, where ω_p is the plasma oscillation frequency given by $\omega_p = \left(n_e e^2/\varepsilon_0 \gamma m_e\right)^{1/2}$. Here, n_e is the plasma electron density, and the relativistic factor γ is related with the laser intensity by $\gamma = \sqrt{1 + a_0{}^2}$. Hence, the on-axis plasma electrons have smaller ω_p and larger η, leading to self-focusing for a Gaussian laser intensity profile in the transverse direction. Relativistic self-focusing is known to occur if the laser power exceed the critical power $P_c = 17\left(\omega_0/\omega_p\right)^2$ GW [9].

Furthermore, the laser plasma can produce a very strong electric field, and such a strong electric field can be used for charged particle acceleration to high energies over a short distance. Generation of a strong electric field results from charge separation between negative electrons and positive ions in the plasma, and the charge separation can be caused by the intense laser pulse. If a short and intense laser pulse propagates in an underdense plasma ($n_e <$ the critical density n_c), for example, it exerts a strong pondromotive force on the plasma, resulting in the generation of a strong plasma wave called a plasma wake wave. The pondromotive force is caused by a spatial gradient of the laser intensity, i.e., $F_p \propto -\nabla\left(n_e I \lambda^2\right)$, in the nonrelativistic regime, and the maximum longitudinal electric field caused by the plasma wake wave is given by $E_z = m_e c\omega_p/e \simeq 96\sqrt{n_e[\mathrm{cm}^{-3}]}$ V/m in the 1-D linear cold-fluid limit [11]. This result gives an extremely strong electric field of $E_z \simeq 96$ GV/m for $n_e = 10^{18}$ cm^{-3}. If the laser intensity is high enough, the plasma wave becomes nonlinear and the so-called wave-breaking can happen, limiting the maximum electric field. The wake wave follows the laser pulse propagating in the plasma, so its velocity is almost the group velocity of the laser pulse $v_g = c(1 - \omega_p^2/\omega_0^2)^{1/2}$. The wakefield is extremely strong and it travels at nearly c, so the laser wakefield acceleration (LWFA) is ideal for electron acceleration. This kind of a wake wave/wakefield can be generated either by using a laser pulse or a high-energy charged-particle (electron or proton) beam pulse. In the case of a high-energy charged-particle beam pulse, the plasma electrons are pushed almost radially by the charged particles, resulting in the generation of a moving plasma wake wave.

If a high-intensity laser pulse is sent to a thin (for example, ~ 1 μm) solid film, the solid material will change to an overdense plasma ($n_e > n_c$) immediately. In this case, the plasma electrons will be pushed backward by the pondromotive force of the laser pulse while the ions in the plasma will not move in such a short time scale due to their heavy mass. Hence, the electrons and the ions are separated, leading to an extremely strong longitudinal electric field. As a result, some protons/ions on the surface of the thin film can be accelerated to high energies. This is called the target normal sheath acceleration (TNSA) [12], and it is a basic proton acceleration mechanism using an overdense plasma. In addition to TNSA, there are some other proton/ion acceleration mechanisms like the radiation pressure acceleration (RPA) [13], where the radiation pressure of an ultraintense laser pulse is directly used for proton/ion acceleration.

There are many other interesting laser plasma phenomena. For example, if a high-power laser pulse is focused in gas (or on a thin solid target), it can produce a strong THz pulse [14]. Besides, a long laser pulse can be converted to an intense short pulse by the Raman backscattering mechanism [15], the details of which will be described later. X-rays can also be produced by various mechanisms in a laser plasma, including the betatron radiation in laser wakefield acceleration [16], bremsstrahlung radiation, etc. In the following sections, some research activities and results for those phenomena will be described.

3 Electron acceleration by a wakefield in a plasma

As mentioned in the previous section, the wakefield in a plasma can have an extremely strong electric field (~ 100 GV/m) under typical experimental conditions, for example, $n_e = 10^{18}$ cm^{-3}. This acceleration gradient is three orders of magnitude higher than that of RF-based conventional accelerators. As an example, the acceleration gradient of 100 GeV/m can give an energy of 1 GeV in 1 cm and 10 GeV in 10 cm. Hence, the acceleration distance can be much shorter for high energies, compared with conventional accelerators, leading to the possibility for development of table-top high-energy particle accelerators. So far, diverse electron acceleration research has been carried out in Korea, including the plasma source development, electron acceleration by LWF, LWFA-based compact light sources, proton-beam-driven electron acceleration, etc. The results are described in this section.

3.1 Plasma source development for laser wakefield acceleration

In LWFA, a plasma source is a vitally important component and diverse plasma sources have been developed at GIST and PAL. They include a supersonic gas jet, a gas cell, and a discharge gas cell. Each source has cons and pros. For example, a supersonic gas jet is simple and easy to use, but it often has a shock wave, leading to an unstable gas density profile along the direction of laser propagation. A gas cell has a main advantage of a gas density stability, but the diffraction problem is inevitable in a gas jet and a gas cell. Hence, a discharge capillary waveguide is a good choice for suppression of the diffraction problem, leading to a longer acceleration length and a higher electron energy in LWFA.

Figure 3 shows the experimental result for transmission of laser pulses in a discharge capillary waveguide, which was performed at the Department of Physics and Photon Science, GIST [17]. In this experiment, a 15-mm-long cylindrical capillary waveguide was used, where hydrogen gas of 50–200 mTorr in pressure was injected into the two feedlines in the capillary with different pressures and a high voltage up to 30 kV was applied to the capillary for electrical discharge. This produces a parabolic-like plasma density profile in the radial direction, providing a focusing effect for the diffracting laser beam. Figure 3a indicates that the transmission of the laser pulse is about 90% when the peak discharge current is over 200 A. This result implies good guiding in the discharge capillary waveguide. Figure 3b shows that a

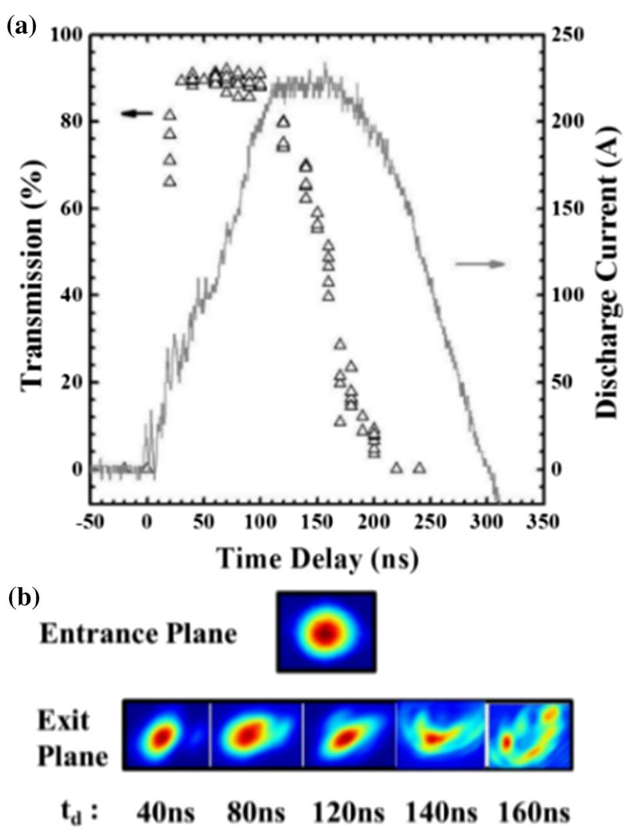

Fig. 3 **a** Transmission of laser pulses in a discharge capillary waveguide as a function of time delay. The solid line shows the discharge current in the capillary hole, and the triangles represent the laser energy transmission with 20 ns intervals. **b** Output laser pulse images at the focus and at the exit of the capillary hole for various time delays [17]

fairly good (round) laser beam is produced by the capillary waveguide when the transmission is high (~ 90%).

A capillary gas cell was also developed for LWFA. In the gas cell, two different gas pressures were applied to the two gas feedlines, leading to an upward density profile. Detailed experimental results, including the longitudinal plasma density profile in the gas cell, are described in Ref. [18]. Extensive simulation studies were also performed to investigate the laser pulse propagation in a hydrogen gas cell. Figure 4 shows the PIC (particle-in-cell) simulation results obtained using the EPOCH code [19], showing the laser pulse propagation for the given gas density profiles. The simulation results indicate that the laser pulse can be self-focused in the hydrogen gas for a high intensity of $I_0 = 4 \times 10^{17}\ \mathrm{W/cm^2}$, while at a low-intensity laser pulse of $I_0 = 2.5 \times 10^{14}\ \mathrm{W/cm^2}$, it is not self-focused and the ionization-induced diffraction is dominant.

A hydrogen gas cell with a length of 15 mm was used for a LWFA experiment with the 20 TW Ti:sapphire laser system at GIST. Figure 5 shows the experimental results using the gas cell, where only a 15 TW peak power was used. For density tapering along the longitudinal direction, different gas pressures were applied to the gas feedlines. The experimental results in Fig. 5 show that quasi-monoenergetic electron beam pulses can be generated at energies between 130 and 250 MeV and that evidently the density tapering effect does occur [20]. In other words, higher density tapering produces higher electron energies (II and III), compared with the untapered case (I). Charge measurement shows that fairly high charges above 100 pC are generated for those three cases. In these experiments, the laser pulse duration was rather long (about 40 fs) compared with the plasma wavelength λ_p for the given densities, so some electrons, especially in the tail of the laser pulse, may have directly interacted with the laser field, contributing to higher energies to some extent.

A new type of gas-filled discharge capillary, which consists of a one-body sapphire block with holes for gas flow, was developed at PAL, and it is shown in Fig. 6. In this design, the capillary is simple in structure and the fabrication is easy, so that there is no concern about the possibility of gas leaks. The designed capillary was already tested for LWFA, and it could generate a stable 300 MeV electron beam by using a 7 mm length and 1 mm hole capillary without an electrical discharge and a 150 PW laser system at IBS/APRI/GIST. For the purpose of a plasma lens which can provide a much stronger focusing force compared with conventional quadrupole magnets, the discharged capillary system was also tested with a current of 100 A and nitrogen gas. PIC simulations for the plasma lens show that a high-energy electron beam can be focused to ~ 5 μm from ~ 100 μm with a plasma current of 50 A, where the PIC simulations were performed with a code developed by UNIST and PAL.

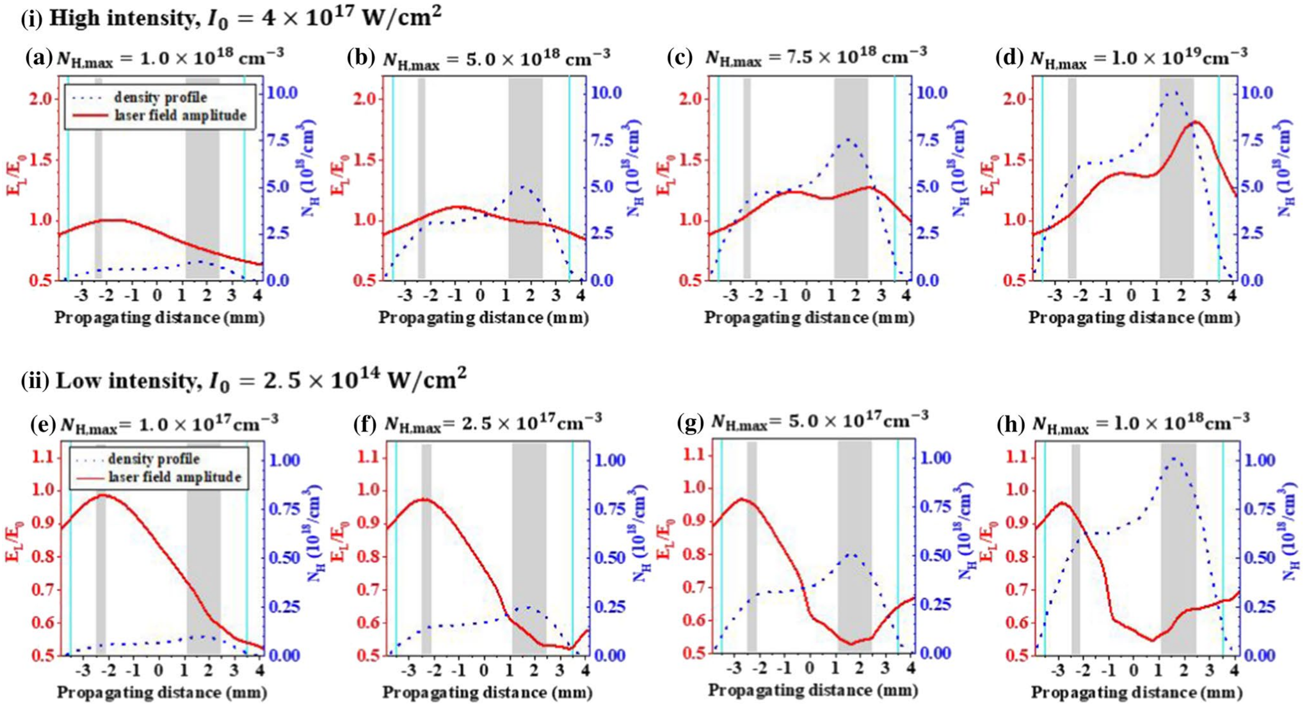

Fig. 4 Laser pulse propagation in the capillary, showing the EPOCH code simulation results: (i) $I_0 = 4 \times 10^{17}$ W/cm^2 (fully ionized) and (ii) $I_0 = 2.5 \times 10^{14}$ W/cm^2 (partially ionized). Note that the high-intensity laser of $I_0 = 4 \times 10^{17}$ W/cm^2 is self-focused in a high-density plasma as shown in **c** and **d**, but not in a low-density plasma (**a**, **b**) [18]. Note that the same density profile is used for all PIC simulations although the maximum density varies

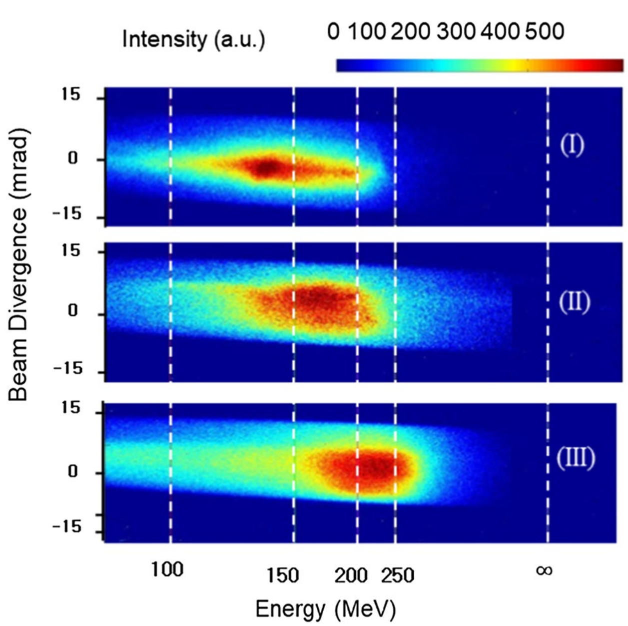

Fig. 5 Electron beam energies from the laser wakefield acceleration experiment using a density-tapered gas cell. In the figures, the input gas pressures at the first and the second gas feedlines were as follows: (I) 2.5×10^{19} cm^{-3}/2.5×10^{19} cm^{-3}, (II) 2.5×10^{19} cm^{-3}/2.7×10^{19} cm^{-3}, and (III) 2.5×10^{19} cm^{-3}/3.0×10^{19} cm^{-3}, respectively [20]

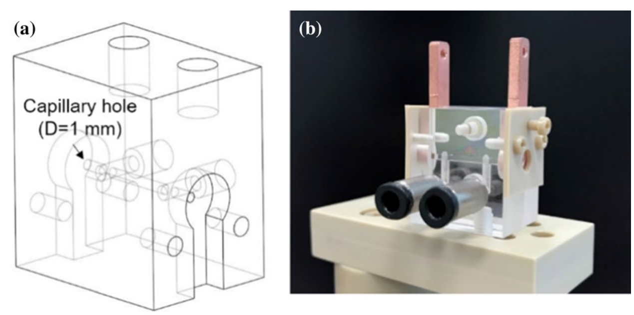

Fig. 6 New gas-filled discharged capillary plasma source at PAL. **a** The 3D drawing shows the capillary, which is a one-body structure. The capillary has a hole diameter of 1 mm and 15 mm in length, and the overall size is 15 (wide)×22 (height)×20 (length) mm^3. **b** Picture of the capillary with electrodes and gas feed lines installed on the PEEK base mount

3.2 Electron acceleration by self-modulated laser wakefield acceleration

For resonant wakefield acceleration (R-LWFA or LWFA), the laser pulse duration should be similar to the plasma wavelength, i.e., $c\tau \simeq \lambda_p$, where τ is the laser pulse duration. If the laser pulse is much longer than the plasma wavelength, i.e., $c\tau \gg \lambda_p$, the Raman forward scattering instability [21] occurs. In this situation, the long laser pulse is split into shorter pulses with spacing of λ_p, and a strong plasma wave can be excited by the periodic laser pulses. Some background plasma electrons can be injected into the acceleration phase of the plasma wave and accelerated. This is called the self-modulated laser wakefield acceleration (SM-LWFA).

The first electron generation experiment using a high-power laser and plasma in Korea was performed at KERI, where SM-LWFA experiments were performed with a 2 TW laser system around 2005 [4]. For the experiments, a supersonic He gas jet and a 2 TW/700 fs laser system, which is a hybrid system of Ti:sapphire (oscillator) and Nd:glass (amplifier), were used. The He backing pressure was in the range of 30 to 60 bars, so the SM-LWFA condition of $c\tau \gg \lambda_p$ is satisfied. Figure 7a shows the Raman forward scattered light, the first and the second anti-Stokes sidebands, and the original Nd:glass laser wavelength of 1.054 µm when the 2 TW/700 fs laser pulse was focused in the He gas jet. This result implies that the Raman forward scattering instability occurred and that a self-modulated laser wake wave was generated. Figure 7b shows that the SM-LWFA experiment generated an electron beam with energies of 4.3 ± 2 MeV.

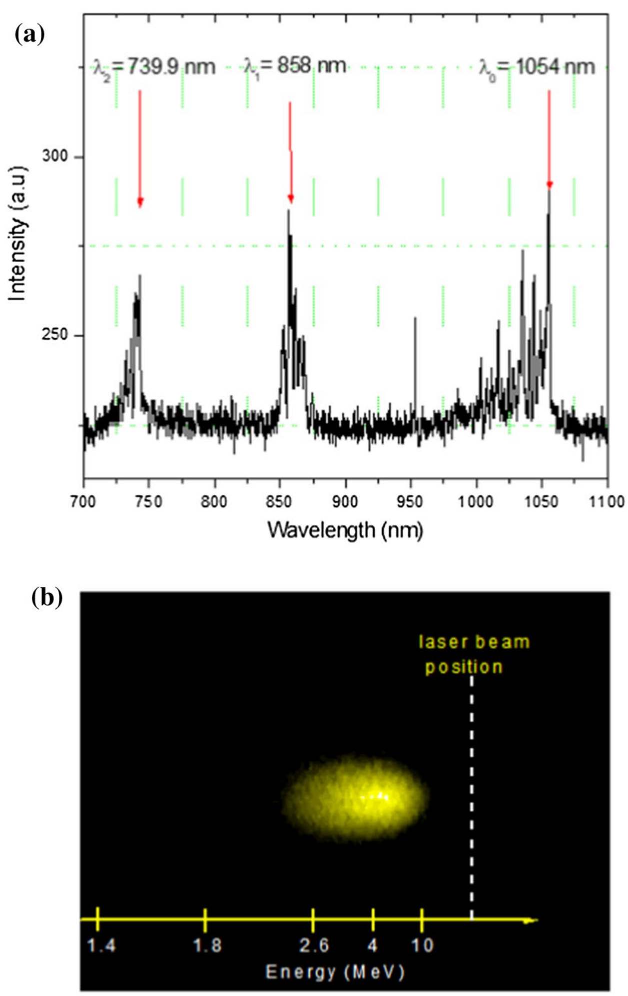

Fig. 7 **a** Raman forward scattered light with anti-Stokes sidebands in SM-LWFA. **b** Electron energy spectrum by a dipole magnet (B = 0.3 T), where the beam energy is 4.3 ± 2 MeV [4]

3.3 Laser wakefield acceleration for very high-energy electron beam therapy

Radiation cancer therapy devices are developed in the direction of minimizing the exposure of normal cells to radiation and reducing side effects by concentrating radiation on tumors. In particular, in the 2000s, theoretical research on treatment methods using very high-energy electron (VHEE) beams began [22, 23]. This method has several advantages that existing radiation therapy machines do not have. In a therapeutic point of view, VHEE beams can penetrate deep into the human body, so there is little distortion of the dose profile due to the air cavity inside the body. For these reasons, the treatment efficiency can be increased by configuring the irradiation direction of VHEE beams in several directions without limiting the structure of the human body [24]. This dosimetric property can be applied to therapeutic treatment planning. As in Ref. [25], the dose profile at different organs was calculated. Based on the Monte-Carlo simulation, the dose to normal tissue close to the tumor was lower than it was in the dose of X-ray therapy. A treatment plan using an electron beam from a laser accelerator was also attempted [26]. More localized energy deposition for VHEE beams compared with X-rays can reduce the side effect during the therapy. Another advantage is the improved control of the irradiation direction. Existing radiation therapy machines have mechanically adjusted the position of the linear accelerator to control the irradiation direction. The shape of the irradiation site has been adjusted by using a large multi-leaf collimator. These methods increase the size of the equipment and cause life-span problems. VHEE beam treatment uses light electrons, so the irradiation position can be precisely adjusted using an electromagnet, and the shape of the irradiation can be made by scanning the beam position, thereby solving such problems. For this treatment device, a small high-energy electron beam accelerator with an energy of 50–250 MeV is essential. Typical RF-based accelerators are difficult to develop in practice due to the size and price of the equipment. A laser wakefield accelerator (LWFA) is a good candidate to solve this problem. In order to confirm this possibility, the physical quantities of VHEE beams, such as the dose profile and relative biological effectiveness (RBE), need to be measured [27]. For this purpose, the physical properties of the VHEE beams accelerated by a LWFA were measured.

For tests of the feasibilities of treatment and to determine the physical quantities of VHEE beams accelerated by LWFA, a 16 TW laser at KERI was used to accelerate electrons and to measure the physical quantities by using equipment at Korea Institute of Radiological and Medical Sciences. The laser was focused by an on-axis parabolic mirror with f/# = 17 at a 3 mm long and 2 mm wide gas nozzle, as shown in Fig. 8. At the nozzle, the electrons were accelerated, and the energy and the bunch charge of the electron beams were measured by using a magnet and an integrated current transformer. The maximum electron energy was 250 MeV with an electron density of 10^{19} cm^{-3} [28]. For long-term stable operation of LWFA, the electron energy was controlled to 100–200 MeV because measurement of the physical quantities of VHEE beams requires more than an hour irradiation to increase the accuracy of the measurement. After the LWFA, a tough phantom consists of solid plastic with a mass density similar to that of water was used in place of a human. An EBT3 film was used to measure the dose profile because of the lack of ion chamber in electron energy range. Before the experiment, the film sensitivity was measured by using the electrons from a clinical linac. The RBE was measured by using the survival fraction of cells receiving different doses.

Figure 9 shows the results for the physical quantities of VHEE beams from LWFA. The depth-dose profiles are in Fig. 9a, b for electron energies of 120 MeV and 170 MeV, respectively. Due to the high electron energy, a dose distribution in the form of a pencil beam with small dispersion was observed, and the dose was delivered to a deep place. The maximum dose was almost linear in the total electron charge so the total dose could be controlled by using the charge deposited to the cell for the RBE measurement. The survival fraction was measured by counting the living cell after the exposure as shown in Fig. 9c. By this method, the measured RBE was 1.2 ~ 1.3, which is higher than the typical X-ray value (RBE = 1). The measurement indicates that the VHEE beam of the LWFA shows physical properties similar to those of the particles used in the typical treatment device, which increases the feasibility of using VHEE beams in therapy systems. Another advantage according to the measurement is that the VHEE beam can focus energy on tumors and minimize exposure to surrounding healthy organs by using a

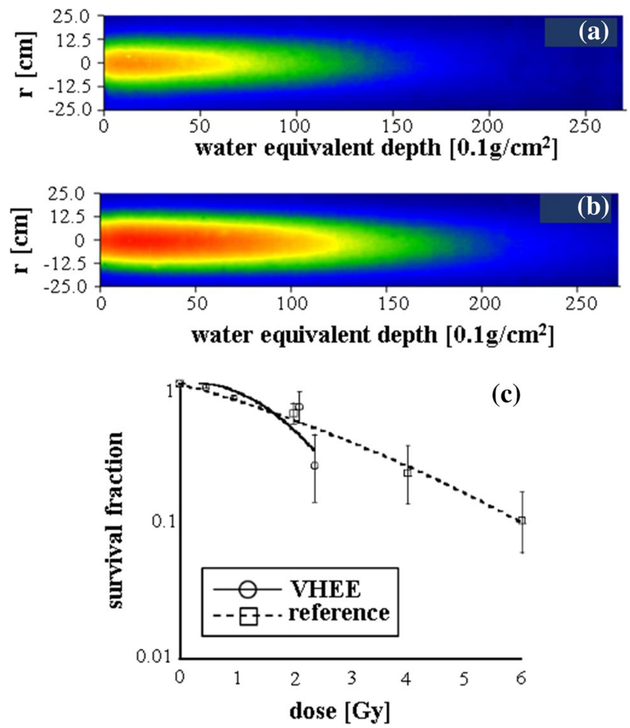

Fig. 9 Measured physical quantities of VHEE beams. **a**, **b** Show the depth-dose profiles for electron energies of 120 and 170 MeV, respectively. **c** Shows the measured cell survival rate for different doses as obtained from RBE calculations

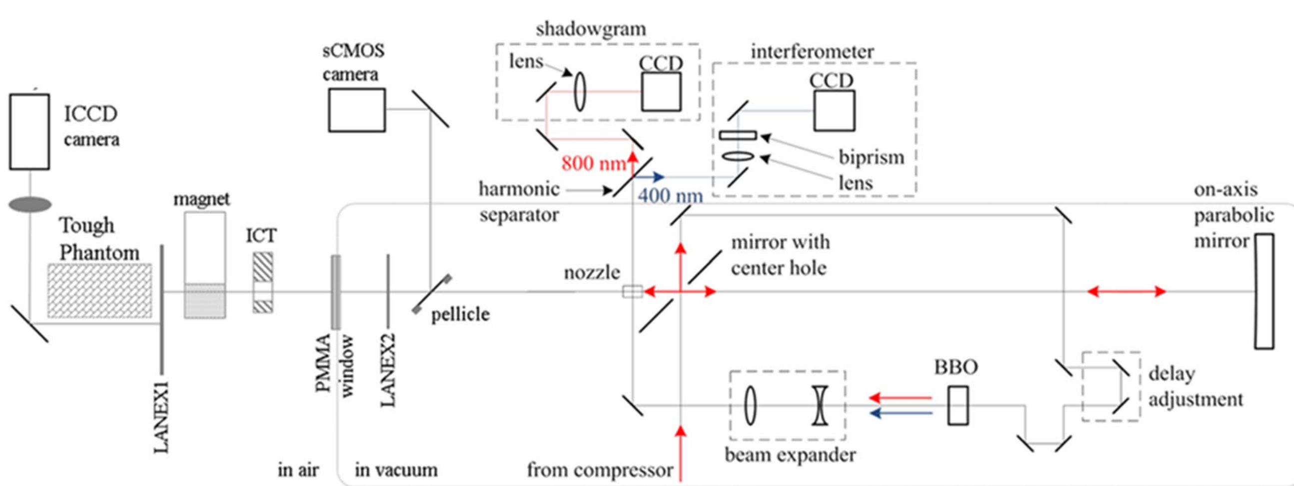

Fig. 8 Experimental setup for measurements of the physical quantities of the VHEE beams from LWFA. The magnet for the electron measurements was removed during the measurement of the physical quantities. Details of the LWFA setup are given in Ref. [28]

well-collimated electron beam. Thus, the VHEE beams from LWFA can be used for a safer and smaller therapy system.

3.4 Compact light source research using laser-accelerated electron beams

The research and development on compact light sources has been under way using a 30 TW Ti:sapphire laser system at KAERI developed to be utilized for laser electron or ion acceleration. Generations of ultrashort gamma-rays via Bremsstrahlung using a Ta target and a THz pulse via transition radiation using multifoil radiator were demonstrated using gas-jet targets, and compact UV and soft X-ray sources via dipole or betatron radiations are under development using metallic targets in collaboration with KAERI and Korea University, Sejong campus.

In the 30 TW laser system at KAERI, a pulse energy of 1.1 J is typically achieved with three staged amplifiers when using a total pumping energy of 4 J from two 2nd harmonic Nd:YAG lasers. The limitation on the laser pulse energy is mainly due to the size of gratings presently installed. A new set of gratings for compressing the chirped, amplified pulse is required to increase the laser power. In general, 60% of laser pulse energy is delivered to the plasma target, corresponding to a 25 TW peak power for a laser pulse with an energy of 1.1 J and a pulse duration of 27 fs.

The plasma source can be generated using a gas-jet target or a solid target. The usage of solid targets has been suggested to realize high-vacuum and high-repetition-rate operation for compact synchrotron sources. In a gas-jet target, a supersonic jet through a tiny orifice can easily form uniform distribution of plasma density along the optical axis of fs laser, but in each shot the vacuum is degraded due to quite long opening time (e.g., several milliseconds) of the solenoid valve with a high backing pressure (e.g., 40–60 mbar). Compared to gas jets and/or capillary gas cells, the amount of plasma plum via ns or ps laser ablation on a solid surface is negligibly small to keep high vacuum. For a helium gas-jet target, the electron plasma density is only twice of helium density after ionization by a high-intensity laser pulse. For a solid target, such as an aluminum, the electron plasma density reaches at least ten times of aluminum ion density. The laser-ablated plasma ions initially in lower charge states are ionized to highly charged states by an intense, fs laser (main laser), increasing the plasma density sufficiently large enough for LWFA. The vacuum of target chamber was confirmed to be kept constant during the generation of laser-ablated aluminum.

A 1.06 mm and 8 ns Nd:YAG laser pulse (ns laser pulse) is irradiated on an Al target to generate the pre-plasma. An elongated distribution of the plasma density is managed using a bi-prism and a cylindrical lens [29]. The channel length can be adjusted by changing either the diameter of the collimated laser for laser ablation or the length of metallic target along the direction of propagation of the main laser. The arrival time of the main laser pulse after generating the pre-plasma can be adjusted by changing the Q-switching time of ns laser. With the aluminum target, the electron was accelerated when the delay time was between 120 and 140 nsec and the height from the target surface was confined to 500 μm $\pm$ 50 μm. The focal position of the ns laser due for a cylindrical lens can be adjusted to improve the uniformity and change the plasma density slightly. The position of the bi-prism can be adjusted for best uniformity along the longitudinal direction.

For plasma diagnostics, two CCD cameras are installed: one for capturing the interferogram due to plasma and the other for monitoring Thomson scattering. For the electron beam measurements, an integrated current tansformer (ICT) and Lanex screen with a 12 bit CCD camera are installed. For the measurement of energy spectrum of electrons, a C-shaped dipole with a permanent magnet including an iron-bar added in side is placed between the Al pinhole and the Lanex screen. The magnetic field strength in the gap can be adjusted by displacing the position of side iron-bar.

3.4.1 THz radiation using a multifoil radiator

The multifoil radiator for THz radiation and the Ta plate for Bremsstrahlung radiation can be mounted after a 50 mm thick aluminum foil at 45°, which is used for blocking the transmitted laser and hot electrons and ions. The THz pulse is emitted 30° off-axis from the propagation direction of the electron beam and is delivered through the crystal window after THz collimation and filtering by optics. The enhancement of THz radiation with a multifoil radiator was demonstrated using 50—60 MeV electron beams generated with a gas-jet target (1 mm dia. nozzle). The THz radiation with 70 sheets of Ti foils was increased about 12 times compared to that with 2 foils [30], as shown in Fig. 10. The pulse duration was 30 fs as measured by using a second-harmonic auto-correlation system.

3.4.2 Ultrashort gamma-ray generation with a Ta plate

Gamma-ray generation was demonstrated using a 25–30 MeV electron beam generated by using a gas-jet target (1 mm dia. nozzle) and fs laser with a pulse energy of 420 mJ at the target. Because the pulse duration of gamma-rays should be several tens of femtosecond, detecting the spectrum by using 2″ NaI detector (Ortec) is hard. However, with reduced the gating time, the ratio of high-energy photons greater than 2 MeV to the background signal is increased, indicating the generation of high-energy gamma-rays with energies up to 30 MeV. The specifications of ultrashort gamma-rays for applications may be calibrated

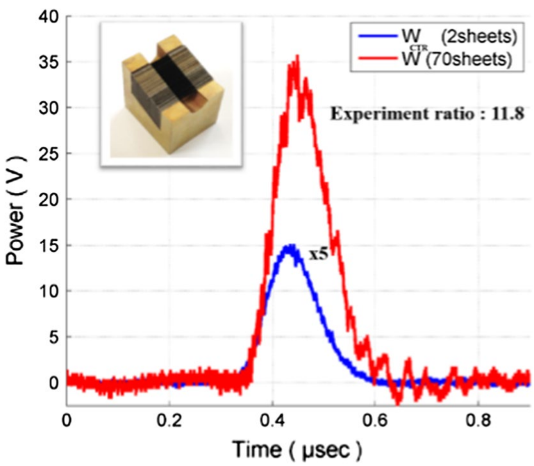

Fig. 10 Enhancement of THz power by using a multifoil radiator. (red) THz power from 70 foils and (blue) THz power from 2 foils [30]

using the simulation results for the well-known (g,n) reaction. According to the simulation results, the (g,n) reaction activated by Bremsstrahlung radiation was insensitive to the energy spread of electron beam, giving similar results for both 5% and 10% spread. The decay spectrum of the ^{197}Au(g,n)^{196}Au reaction after activation of Au with 1000 shots was measured. The decay lines, such as 355.7 keV, 333.0 keV, and 426.0 keV, are in agreement with the calculated ones, and the half decay time measured is about 6.2 days [31].

3.4.3 High-vacuum laser electron acceleration and synchrotron radiations

A compact light source, especially in the range between deep UV and soft X-rays, should be operated in high vacuum. It can be realized using metallic targets as mentioned. The laser-ablated plasma density is increased via laser ionization as long as the main laser intensity is greater than the ion appearance intensity. According to the ion appearance intensity, the final charge state of the Al ions may be Al^{11+} for a main laser intensity of 10^{19} W/cm^2. The pre-plasma ablated by a ns laser pulse with its energy of 240 mJ was increased by a factor of 2.5 [29]. The amount of Al ions ablated is determined by the condition of the metal surface and the intensity of the ns laser. The irradiated surface, being annealed by heating due to the laser pulse, released insufficient ions to reach the desired final plasma density. A disk-type target and its surface polishing system are being developed for operation with a high-repetition rate and improving the reproducibility of the pre-plasma under the same condition, as shown in Fig. 11.

The ionization process causes ionization diffraction of the main laser in the plasma, reducing the guiding length. The maximum energy of the electron beam is lower than that for a helium gas-jet. However, it increases the electron injection into the wake cavity. According to 2D PIC simulations (EPOCH code [19]) using a 60 TW laser with its waist of 7 mm for $n_{ef} > 10^{19}$/cm^3, the central energy was reduced from 165 to 105 MeV with a 30% energy spread as the density was increased. At 0.7×10^{19}/cm^3, the peak energy of 272 MeV with a 3.5% energy spread was estimated. So far, a peak energy of 50 MeV, on average, has been obtained using a 25 TW main laser in experiments.

The 360° bending magnet for a compact synchrotron light source was designed (Fig. 12). It is comprised with a ring-shaped pole and permanent magnet blocks [32]. Two shapes of the magnet block were used, instead of one ring-shaped magnet, to reduce the cost. It gives a sinusoidal modulation of the magnetic field inside the dipole. The number of pairs

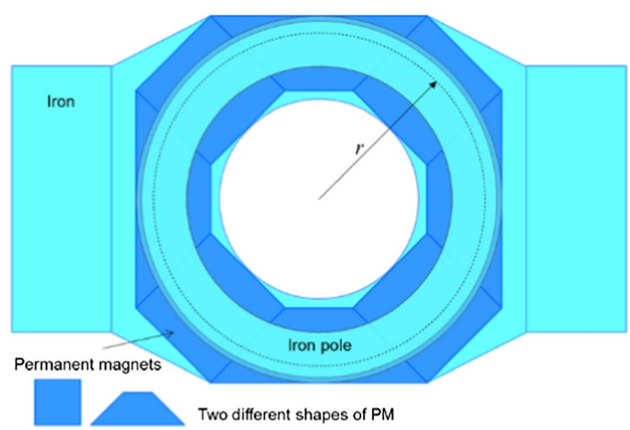

Fig. 12 Schematic of the 360° bending magnet (Ref. [32])

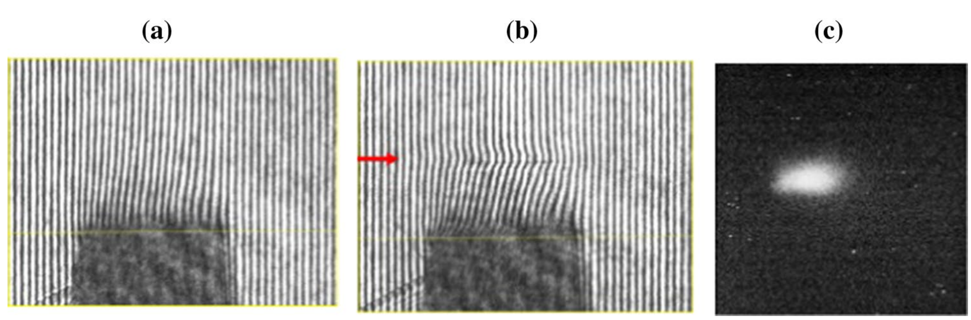

Fig. 11 Interferograms of the pre-plasma and the main plasma for an aluminum target: **a** interferogram of the pre-plasma, **b** interferogram of the main plasma, and **c** image of the electron beam

corresponds to the number of modulation periods and the modulation depth depends on the magnetic field strength. For a stable circular orbit, the angular divergence of the electron beam injected to the dipole should be small enough, satisfying $x_0' \leq B_1\rho_0/n$, where B_1 is the field modulation with respect to the dipole field B_0, ρ_0 is the radius of the electron orbit, and n is the number of modulations in one turn.

The LWFA using metallic targets may be a good candidate for producing betatron radiation. Figure 13 shows the difference of injected electron beam between helium and aluminum targets. With a fixed focusing position of the fs laser, the starting point of the injection is almost same for both, but the injection continued slightly longer and more for the Al target. For the Al case, the wave-breaking point is slightly away from the optical axis and the oscillation of electron beam inside the cavity is larger. 2D and 3D PIC simulations by using the EPOCH code are underway with a new target design for the compact Soft X-ray source by adding narrow Ti film near the injection position.

3.4.4 External injection for the LWFA-based future FEL

For a future compact X-ray free-electron laser (XFEL), a laser plasma accelerator is a promising candidate [33]. However, the present electron beam quality of the laser plasma accelerator is poor, i.e., a few percent of energy spread, low stability and low reproducibility, which does not satisfy the demanding criteria for the XFEL. If the requirements are to be met, the electron beam needs an energy spread of 0.1% and an energy jitter of 5×10^{-4} stability, which is difficult to achieve in the current level of LWFA. Therefore, one of the most promising ways to overcome this limitation is to use the electron beam of good quality from the RF photocathode as a seed beam for laser plasma accelerators. The PAL-ITF GUN-II beamline of the RF photocathode can produce a beam energy of 70 MeV, an energy spread of 10^{-3}, a jitter of a few tens femtoseconds, and a low emittance of 0.2 mm-mrad, which can be an excellent seed for the LWFA. The PAL-ITF is, thus, the place to demonstrate the most reliable LWFA with an external injection scheme.

In LWFA of an external injection scheme, an external electron beam has to be well-guided into the plasma wake to preserve the beam emittance. The focusing force inside the plasma wake is very strong, resulting in a beam size of a few micrometers for betatron motion. Therefore, the externally injected beam should be matched to the intrinsic betatron motion in the plasma wakefield. Thus, it is crucial that the electron beam size should be matched to enter the plasma wake to preserve the beam emittance. For good matching conditions, one way is to use a slowly increasing plasma ramp to minimize the emittance growth. Another direct method is to focus the electron beam down to a few micrometers at the entrance of the plasma by using a plasma lens [34]. A key component to meet these conditions is a gas-filled discharged capillary plasma source with a well-controlled plasma density gradient. Figure 14 presents the future plan for LWFA with matched external injection from the RF photocathode GUN-II. For further diverse experiment schemes, some upgrades will be done. A bunch compressor will be installed soon to produce a high beam current and short electron beam duration. The high-power laser system will be built as the existing laser system does not have enough power for the LWFA. If the upgrades are done, the electron beam will have a higher current and it can be also used as a driver to excite an electron-beam-driven plasma wake wave for the so-called plasma wakefield acceleration (PWFA).

3.5 Beam-driven plasma wakefield acceleration

Due to the lack of experimental facilities that can provide high-quality high-intensity driver beams [35], beam-driven plasma wakefield acceleration (PWFA) activities have been somewhat limited in Korea. In US and European countries, on the other hand, steady investment and progress have been made in this field [36]. Examples of such activities include Advanced Wakefield Experiment (AWAKE) at CERN, FACET-II at SLAC, and FLASHForward at DESY, to mention a few. Among various PWFA experiments, the AWAKE is noteworthy in that it uses protons as a driver beam [37]. The proton beam from Super Proton Synchrotron (SPS) has

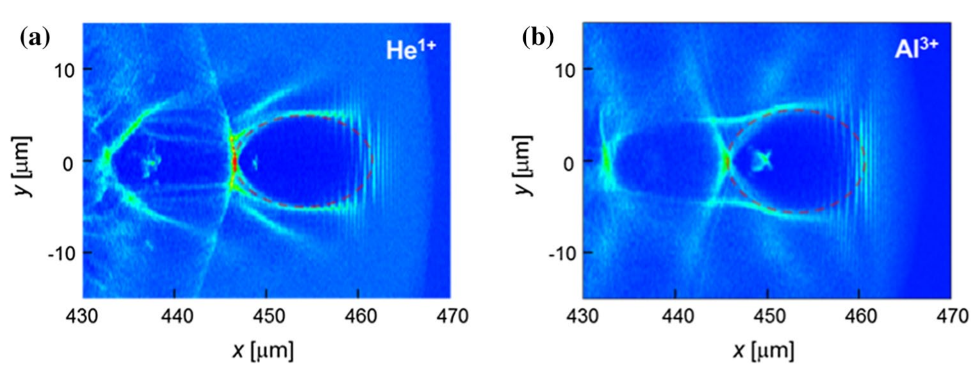

Fig. 13 Electron density maps for **a** helium target and **b** aluminum targets as obtained using 2D PIC simulation. The snapshots are captured at 1.5 ps for both plasma targets having the same final electron density of 1.2×10^{19}/cm^3. The color scale of the electron density is the same for both cases

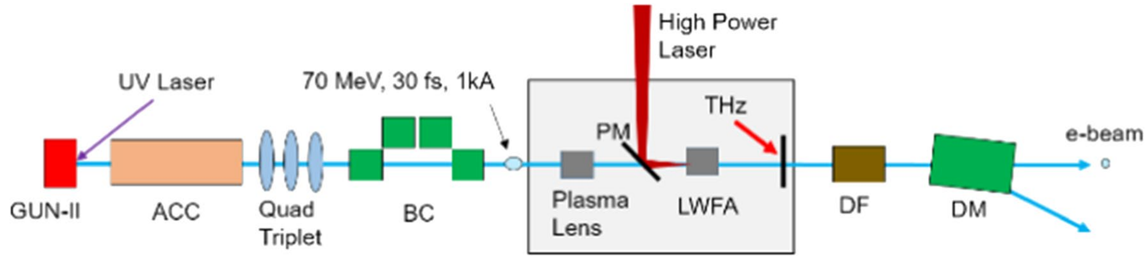

Fig. 14 Schematic diagram of the future upgrade plan for the laser wakefield acceleration with a matched external injection of the stable electron beam from the RF photocathode GUN-II. The abbreviations in the figure are as follows: bunch compressor (BC), plasma mirror (PM), terahertz (THz)

a stored energy of approximately 19 kJ, which is considerably large compared to other wakefield driver sources [38]. Hence, it is expected that a single proton beam can be used to generate the plasma wakefield, sustaining its accelerating gradient without staging. In 2018, the AWAKE team demonstrated electron acceleration through a proton beam-driven plasma wakefield up to 2 GeV. An ionization laser with an energy of 450 mJ is used to generate a 10-m-long plasma column from Rb-vapor neutral gas. The proton beam, which is self-modulated inside the plasma source due to a process called seeded self-modulation (SSM), becomes split into micro-bunches and creates the wakefield.

The UNIST research group joined the AWAKE collaboration in 2016 and has been actively involved in the experimental programs since then. The UNIST group mainly focused on the commissioning and the characterization of the witness electron beam injector used in the AWAKE Run 1 experiment [39]. In addition, an optimization study of the beam transfer line for external injection [40] and simulations of electron bunch seeded self-modulation [41] are in progress for the upcoming Run 2 experiment. Apart from the scope of the AWAKE, the UNIST group also investigated several general issues relevant to beam-driven wakefield acceleration schemes such as longitudinal phase space dynamics during Trojan-Horse injection [42], manipulation of the driver beam by using double emittance-exchange [43], and witness beam focusing with an active plasma lens [44].

In recent years, the possibilities of PWFA R&D using electron beams available in Korean accelerator facilities have been actively discussed. Through the development and operation of the PAL-XFEL, the hard X-ray free-electron laser facility at Pohang Accelerator Laboratory, considerable infrastructure and experience in generating and manipulating high-quality electron beams have been accumulated. For example, the Injector Test Facility (ITF) at PAL can be used as an R&D platform for advanced accelerator concepts, including LWFA, PWFA, structure wakefield acceleration (SWFA), and their combinations. An electron beam focusing experiment using an active plasma lens for application to external injection is currently under consideration. The beam-plasma interaction experiments using a custom-designed arc discharge plasma are in preparation, together with the beam line optimization and detailed particle-in-cell simulation. Additionally, external injection of the electron beam to the laser plasma wakefield or structure wakefield will follow in the near future.

4 Acceleration of an energetic ion beam from a laser-induced plasma

Since the first significant observation of energetic protons [45], energetic ions from a thin film irradiated by an ultra-intense laser pulse have attracted a considerable amount of attention for potential applications to hadron cancer therapy, inertial fusion, and nuclear physics [46–48] because of their compact size. Many efforts have been made to understand the underlying mechanism [49], such as target normal sheath acceleration (TNSA) [12, 45], collisionless shock acceleration (CSA) [50], radiation pressure acceleration (RPA) [13], and acceleration by a resistively induced electric field (ARIE) [51, 52]. Recently, a proton beam with an energy of 100 MeV was observed using a multi-100 TW and petawatt laser system [53, 54]. However, most of the ion beams generated in the laser acceleration show a thermal distribution, exponentially decreasing ion numbers with energy and having a cut-off. In addition, the maximum energy obtained is still lower than the 200 MeV required for the proton cancer therapy.

The possibilities of a quasi-monoenergetic proton spectrum have been experimentally demonstrated from a micro-structured target [55] and a heated palladium target [56], which exhibited energy spreads of 25% for protons and 17% for C^{5+} ions. Those targets used small transverse size and thin layer of target ions on the rear surface of thick metal foils, thus utilizing the electrostatic field at the rear surface of the metal foils or the TNSA mechanism. However, the peak energies are just 1.2 MeV/u and 3 MeV/u for protons and carbon ions, respectively. Other than foil targets, a liquid droplet [57], a hydrogen gas with a laser pulse train [58], and a micro-size plastic sphere [59] have also exhibited non-Maxwellian proton spectra.

The ETRI group has also done research using their 500 TW/30 fs Ti:sapphire laser system. The main research at ETRI is the generation of protons/ions for medical applications, especially cancer treatment, and research is underway.

4.1 Layered-film targets

The main acceleration field in the laser-induced plasma acceleration of charged particles is a surface field, or a sheath field which is built on the surface of a target foil by hot electrons energized by a laser field at the front side and propagated to the rear side, which can be mainly explained by using the TNSA mechanism. On the contrary, the KAERI group has paid attention to the bulk field that is formed inside the plasma by diffusion of the sheath field as the plasma expands. The advantages of the bulk field are that first, it drives ions for longer time, thus leading to higher energy and second, ions driven by the field can be confined at their initial positions, leading to narrow energy spreads. Several types of a layered-foil were proposed as shown in Fig. 15, which are VSDL (vacuum-sandwiched double layer) [60], ILEF (ion-layer embedded foil) [61], and IEDL (ion-enhanced double layer).

An interesting, peaked spectrum from an IEDL target has been demonstrated, as shown in Fig. 16. Even though the shot-to-shot variation is very large due to the preparation of the target foils, it shows that the energy spectrum can be tailored by modifying the structure of the target. Some experimental observations support bulk acceleration, leading to higher energy and a narrower (or non-thermal) spectrum. However, the acceleration mechanism, especially with a high initial plasma resistivity, needs to be understood, and this can be a key parameter to reveal the acceleration mechanism in a layered-foil target [62].

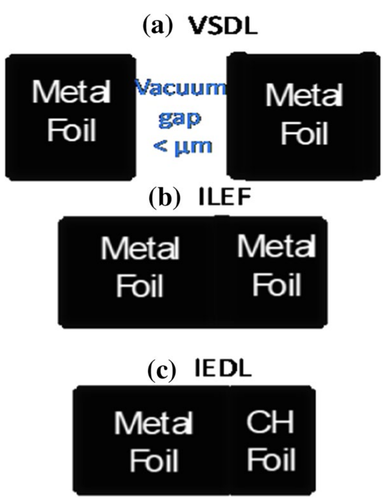

Fig. 15 Various layered-film targets developed at KAERI: **a** vacuum-sandwiched double layer, **b** ion-layer embedded foil, and **c** ion-enhanced double layer

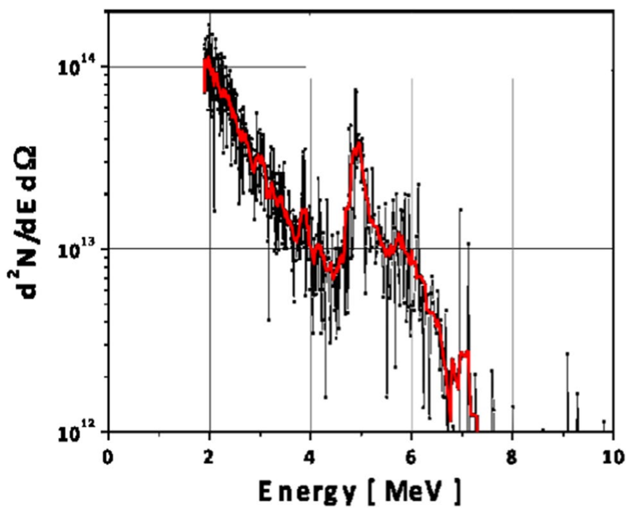

Fig. 16 Demonstration of a proton beam with a peaked spectrum. It was obtained from an IEDL target, Cu-2 mm, and PMMA brushed on the copper surface for a laser pulse of 2×10^{19} W/cm^2 irradiating the copper side

5 High-energy-density plasma

Recent advances in high-intensity short-pulse lasers allow the creation of high-energy–density (HED) plasmas at energy densities above 100 GJ/m^3 [63, 64]. As illustrated in Fig. 17, such conditions are widespread in the universe and in various applications such as planetary science, inertial confinement fusion, advanced laser ablation, and even nanosurgery [65–68]. In the HED regime, warm dense matter (WDM) represents a state where the thermal energy is comparable to the Fermi energy and the ions are strongly coupled [69, 70]. Typically, WDM exhibits temperatures of ~ 1–10 eV and near-solid densities. It lies at the juncture of solid, gas, and low-density plasma, and the investigation of such plasmas could provide a key understanding of the non-equilibrium phase transitions and the energy relaxation processes in extreme conditions. However, in this regime, our physical description is weak because of the complicated interplay of the physical processes from its neighbor states.

5.1 Time-resolved X-ray absorption spectroscopy for warm dense matter research

Over the last decade, the development of time-resolved X-ray absorption spectroscopy (TR-XAS) techniques has been actively pursued at GIST. The X-ray absorption spectrum of matter contains useful information regarding the

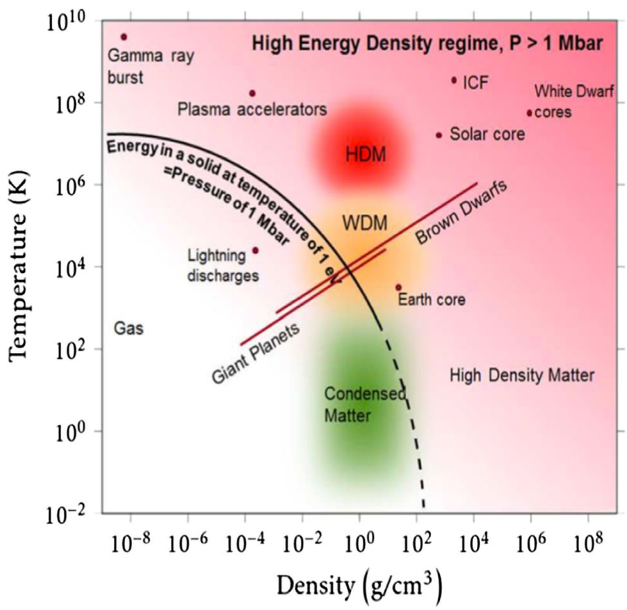

Fig. 17 Phase diagram of high-energy-density matter. Warm and hot dense matter lie at the confluence of condensed matter, gas, and classical plasmas. In this regime, both classical and quantum effects are important, but have not been described adequately. Figure is extracted from reference Ref. [71]

electronic structure and/or local geometry of the matter, which are basic experimental data to understand the fundamental properties of matter. We have sought novel application of TR-XAS in the WDM regime where insufficient fundamental data are a major setback in the further understanding of extreme matter. A series of efforts include the development of laser plasma-based X-ray and extreme ultraviolet sources as well as synchrotron and free-electron laser based diagnostics [72–74] to cover various photon energy ranges and time scales. As an example, the TR-XAS beamline at GIST is shown in Fig. 18. With the 150 TW laser at the Center for Relativistic Laser Science, a broadband soft X-ray source can be generated and used as a probe of a laser heated WDM sample in transmission geometry.

With these diagnostics, the temporal evolution of X-ray absorption and the transient electronic structures of warm dense copper and metallic silicon dioxide have been measured [75, 76]. The thermodynamic properties of WDM, such as the electron–ion coupling rates, heat capacity, and thermal conductivity of copper and iron at temperatures of a few eV have been also reported [77, 78]. These provide unique sets of experimental data to the HED community and shed lights on developing an advanced theoretical description and further improving our understanding of ultrafast excitations, phase transition dynamics, and thermodynamic properties of plasmas under extreme conditions.

5.2 HED plasma produced using an X-ray free-electron laser

The advent of the X-ray free-electron laser (XFEL) allows a light intensity over 10^{16} W/cm^2, which is now feasible in the X-ray regime. Such an XFEL pulse can heat solid samples to temperatures of 10–100 eV to produce ideal HED plasmas to be investigated. The typical deep penetration of X-rays enables a large volume of the target to be heated uniformly. Because of the femtosecond pulse duration, this heating is isochoric with an initial density. These establish well-defined high-density-high-temperature conditions in a larger volume of samples.

Fig. 18 Time-resolved X-ray absorption spectroscopy beamline at GIST. Broadband (200–1000 eV) soft X-ray pulses from a tantalum plasma irradiated by a 150 TW laser pulse are generated in the X-ray chamber. In the sample chamber, a solid target is superheated by a separate femtosecond laser pulse and WDM is formed. The transmitted X-ray probe is dispersed and detected by a spectrometer detector system

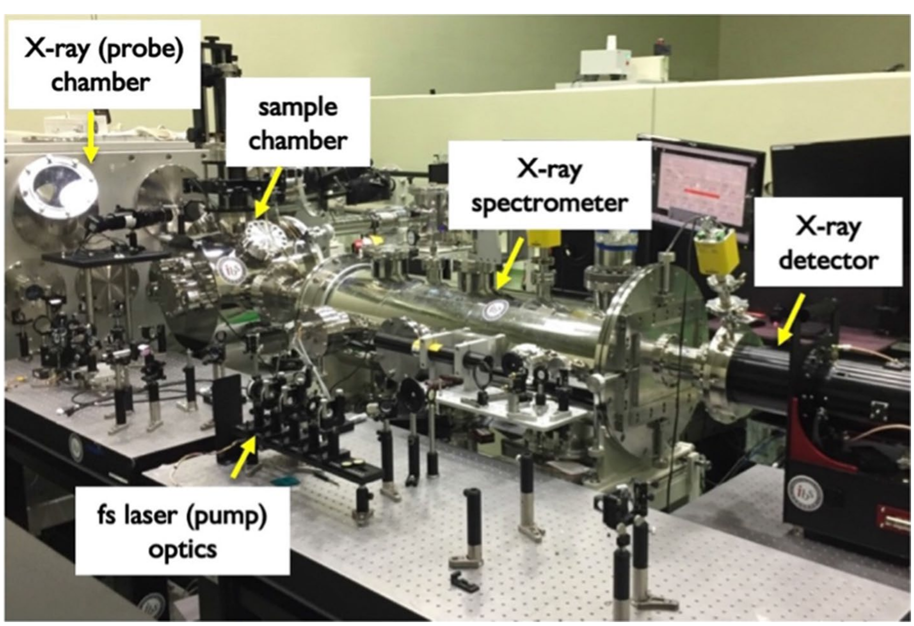

At GIST, we have focused on X-ray emission and absorption spectroscopic studies on intense XFEL – matter interactions and hot dense plasmas created as results. Figure 19a illustrates the general concept of the experiment and gives typical examples of X-ray spectroscopic data for aluminum targets interacting with an X-ray laser at intensities of $10^{16\sim17}$ W/cm^2. K-shell emission (Fig. 19b) spectra indicate that the solid density aluminum plasma has electron temperatures of 100–200 eV [79, 80]. Figure 19c shows the experimental demonstration of saturable and reverse saturable absorption in the X-ray regime [81, 82]. It is noted that the theoretical advances, such as re-evaluation of the ionization potential depression and the collisional ionization rates in HED plasma, should be included in the modeling of these sets of data [83, 84]. The nonlinear responses in the X-ray regime would be of great importance in photonic applications, such as modulating X-ray beams and the development of atomic X-ray lasers.

5.3 Laser cluster fusion

Modern high-power lasers are so powerful that they can be used to study nuclear fusion reactions. In laser-cluster-fusion experiments, intense (> 10^{16} W/cm^2) laser pulses irradiate ~ 10 nm radius spheres of solid density deuterium (called deuterium clusters) [85, 86]. If the incident laser field is strong enough, laser matter interactions result in an explosion of individual spheres, producing energetic deuterium ions. The so-called Coulomb explosion model has been fairly successful in predicting how much the ions gain kinetic energy from the incident laser beam [87–90]. According to the model, electrons within the cluster first absorb the laser pulse energy as deuterium atoms are ionized. The electrons further absorb the incident laser pulse energy and escape from the cluster, leaving a positive charge buildup on the cluster. Subsequently, the highly charged spheres of deuterium ions at solid density undergo Coulomb explosion, and a high temperature (~ 10^8 K) deuterium plasma is produced [90, 91]. The resulting deuterium ions are very energetic, so they can produce nuclear fusion reactions when they collide with each other inside the hot plasma. Nuclear fusion is also possible if energetic deuterium ions run into cold deuterium ions or atoms in the cold background gas [90].

As shown in Fig. 20, energetic deuterium ions colliding each other can produce DD nuclear fusion reactions. Since the fusion cross-section increases very rapidly with ion temperature in the several-keV to several tens of keV region, it is important to know how we can increase the temperature

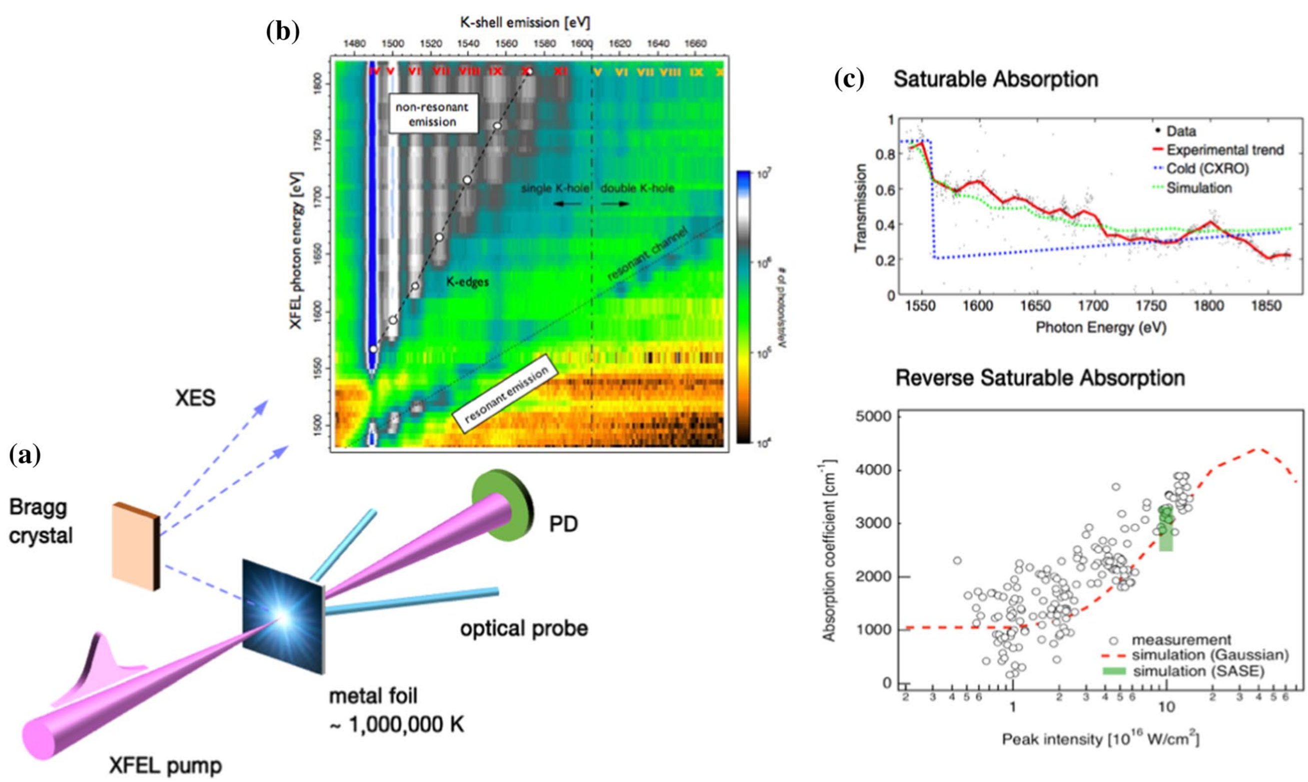

Fig. 19 **a** General concept of the spectroscopic study of XFEL-heated HED plasmas. An XFEL pulse is tightly focused on a solid density target to create WDM and HDM. **b** X-ray emission and **c** X-ray transmission/absorption spectroscopy data to map out the charge states and the ultrafast electron dynamics for X-ray–matter interactions in HED plasmas. The figure is reproduced from Refs. [79–82]

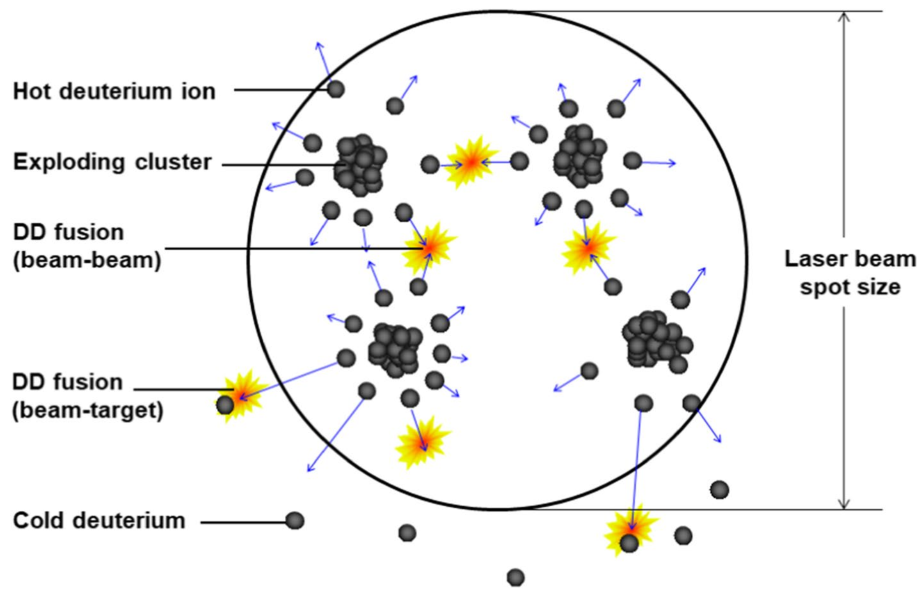

Fig. 20 A schematic diagram showing DD nuclear fusion reactions from exploding deuterium clusters

of the fusion plasmas created by this technique. In recent experiments, we investigated the dependence of the ion temperatures of fusion plasmas on the incident laser intensities. Based on our study of the dependence of fusion plasma temperature on incident laser intensity, we can now produce a deuterium fusion plasma with a specific temperature by controlling the incident laser intensity on a cluster jet. With this technique along with neutron yield measurements and plasma volume measurements, we aim to measure the DD fusion cross-sections directly from laser cluster fusion experiments [92].

6 Laser-plasma-based THz wave generation and applications

Generation of a strong THz wave is a very important research issue. Laser plasmas can be used for that purpose. When a single-color laser pulse [93] or two-color (sum of the fundamental and second-harmonic frequencies) laser pulse [94] is focused in a gas, a strong THz wave pulse can be generated. A good advantage of this method is that the laser plasma is electrically broken down already, so there is no concern about any damage in the THz source. So far, diverse methods for strong THz wave generation and applications have been studied. One of them is the application of the laser plasma-produced THz wave for the plasma diagnostics. The laser plasma-based THz wave is very useful for diagnostics of some plasmas, for example, a tokamak fusion plasma with a density range of 10^{13}–10^{14} cm^{-3}, where THz frequencies have a good coupling with the plasma. Furthermore, the laser plasma-based THz wave has a broad range up to a few THz for the single-color method and tens of THz for the two-color method, which can cover a very wide range of plasma density ranges. Here, one example of the laser plasma-based THz wave generation and applications is introduced [95].

For generation of a strong THz wave, the Ti:sapphire regenerative amplifier at GIST was used. As Fig. 21 shows, the laser pulse with an energy of 3 mJ and a pulse duration of 40 fs was split into an intense pump beam and a weak probe beam. The pump beam goes to the BBO crystal for frequency doubling and overlapped laser pulses of the fundamental and second-harmonic frequencies are focused in air, producing a strong THz wave pulse. This THz wave passes

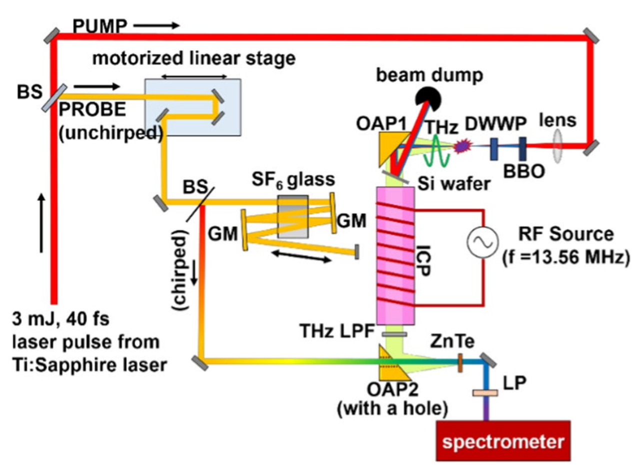

Fig. 21 Experimental setup for THz generation and diagnostics. The pump beam is focused in air for generation of a strong THz pulse and the THz pulse is sent through the plasma. The probe beam is frequency-chirped in the SF_6 glass and overlapped with the THz pulse in the ZnTe nonlinear crystal

through the inductively coupled argon plasma that can produce a density similar to that of typical tokamak plasmas. On the other hand, the probe laser pulse is frequency-chirped in the dispersive material of SF_6 glass, and it is overlapped with the pump beam in the ZnTe nonlinear crystal. Due to the electro-optic effect of ZnTe, the THz wave form with a phase shift from the plasma can be obtained.

BS: beam splitter, GM: gold-coated mirror, OAP: off-axis parabolic mirror, DWWP: dual wavelength waveplate, LPF: low-pass filter, LP: linear polarizer.

Figure 22a shows the frequency-chirped and unchirped pulses of the probe beam, and Fig. 22b shows the measured THz pulse waveform. Here, THz waveforms from two different measurement methods are compared: one is from the THz-TDS (time domain spectroscopy) [96] and the other is from the spectral encoding (SE) method [95], showing similar results. Compared with the THz-TDS method, however,

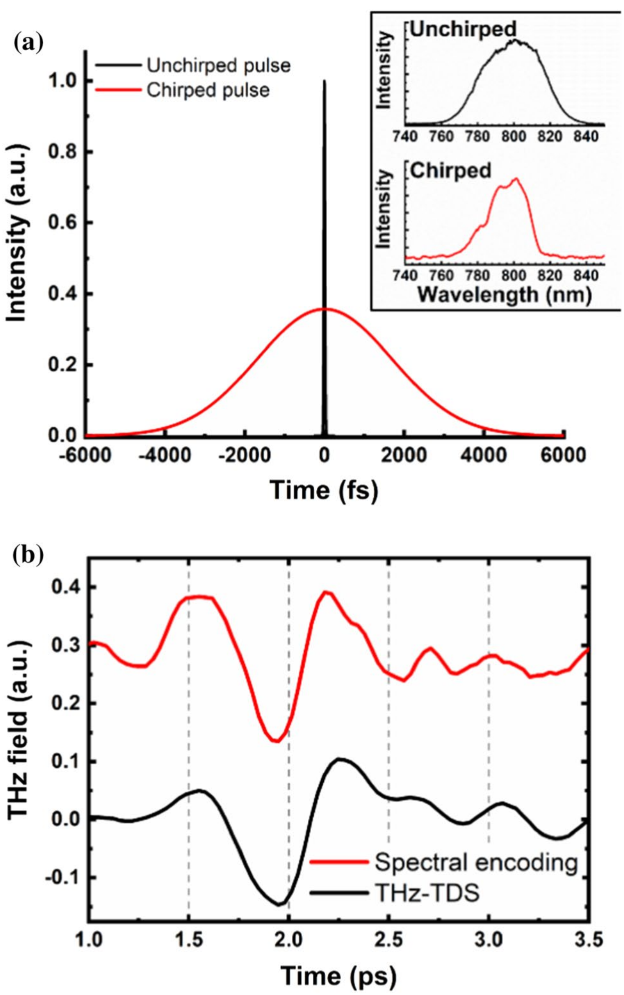

Fig. 22 **a** Temporal profiles of the unchirped and the chirped probe beams (the intensities are in arbitrary unit). Inset: wavelength spectra of the unchirped and the chirped pulses. **b** Comparison of THz fields obtained from the SE and the THz-TDS methods [95]

the SE method has a very important feature. In other words, the SE method can provide plasma density information immediately, while the THz-TDS method takes a minute for scanning the probe pulse over the THz signal. Therefore, the SE-based plasma diagnostic method is better. As this example shows, a laser plasma can be used for the generation and application of a strong THz wave pulse.

7 Plasma optics for laser pulse compression

Most applications from laser plasma interactions exploit the ponderomotive force of the laser pulses to generate periodic structures out of randomly distributed plasma particles. The laser wakefield accelerator is a good example of that. The ability of the lasers in manipulating particular periodic structures in a plasma gives a wide opportunity for using the plasma as an optical component. The periodically modulated density, which is an alternating refractive index, changes the dispersion relation of electromagnetic waves as in the photonic crystals. Depending on the periodicity and amplitude of the modulation, the plasma can be used as a mirror, gratings, or radiation emitter. In the sense that the plasma can generate photons of desired frequency, it can be considered an active photonic device, not just a passive one. The great advantage of using the plasma as an optical device is that a very highly intensity, which is far beyond the damage threshold of regular matter for optics, can be readily handled in the already-broken-down (so no additional damage) state plasma.

The modulated density of a plasma is usually oscillating either with the electron plasma frequency or the ion-acoustic frequency. The oscillating behavior gives a unique feature to the plasma as an optical device. Since the dispersion can be made to alternate over time, the plasma can play the role of an active photonic device that can generate or amplify photons or change the frequency of the photons, in contrast to just being passive optical components for reflection or diffraction. The aspect of the plasma as a photonic device is well demonstrated by backward pulse compression via nonlinear backscatter in a plasma.

The idea of pulse compression [15, 97] is based on the three-wave interaction between the pump, seed, and plasma waves. The scheme of pulse compression using a plasma was motivated by the need for damage-free gratings in the chirped-pulse-amplification technique. The fabrication of the super-large gratings required for the CPA (chirped-pulse-amplification) technique to go beyond currently available petawatt (and almost exawatt) power, has almost reached the technological limit, setting a bottleneck in further development of CPA. The already-broken-down plasma is free from material damage and hence can be useful for pulse compression in the post-exawatt era. The mechanism of

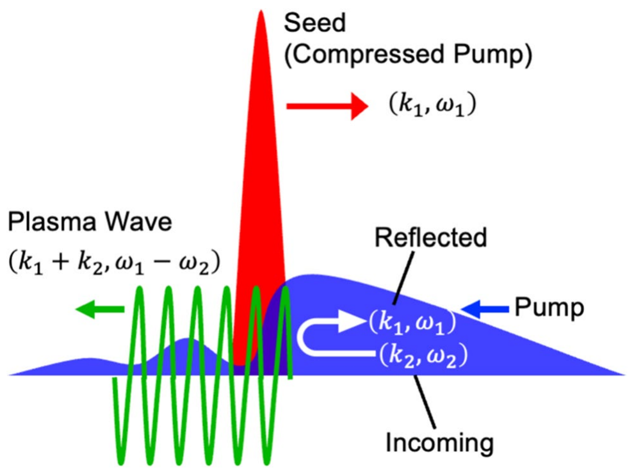

Fig. 23 Schematics of pulse compression in a plasma (green box). The right-going seed (red) and the left-going pump (blue) laser pulses generate a local plasma wave (black)

the plasma scheme of pulse compression can be intuitively understood from Fig. 23. A long pump laser pulse, which should be compressed, is allowed to let propagate through a plasma (from right to left in the figure). At the same time, a short seed laser pulse is made to collide with the pump pulse inside the plasma, with the frequency slightly detuned down from the pump frequency by the amount of the plasma frequency. In the overlap, the ponderomotive force due to the beating of the pump and the seed pulses generates a density modulation with a wavelength roughly equal to a half of the laser wavelength. Here, the plasma density modulation, or just the plasma wave, moves in the direction of the pump with a slow velocity determined by

$$v_{PM} = \frac{\omega_1 - \omega_2}{k_1 + k_2},$$

where the subscripts 1 and 2 represent pump and seed, respectively. With this motion, the pump laser pulse is backscattered red-shifted by the Doppler effect. Because the down-shifted frequency coincides with the seed laser frequency, the scattered pump pulse can add onto the seed pulse, eventually resulting in compression of the pump pulse into a narrow seed pulse. The seed pulse also scatters, but with up-shifted frequency. From the Manley-Rowe relation, energy flows from the high-frequency wave to the low-frequency. The scattering process should satisfy conservations of momentum and energy for each wave.

$$\omega_1 - \omega_2 = \omega_p,$$

$$k_1 - k_2 = k_p.$$

Plasma-based backward pulse compression has been studied for a couple of decades. The state-of-art is 35% pump compression realized in full three-dimensional particle-in-cell simulations [98] (with inclusion of as many realistic effects as possible). Experimentally, the compression efficiency is about ten percent with the Joule-level pulses [99, 100]. The exact reason for the lower efficiency in the experiment is not fully clear yet. The pre-depletion of the pump in the plasma noise is believed to be one major factor that deteriorates the compression efficiency. Also, the grating structure, which is easily broken by the wave-breaking mechanism, can also significantly ruin the compression procedure [101–103]. Incomplete ionization of the gas and accompanying neutral-electron collisions may also be the origin of the lower efficiency, though this effect has not been addressed intensively. If the grating structure is to be more robust, Brillouin scattering, which utilizes the ion-acoustic wave as a grating, is also a very promising variation. In this case, the ion density is also modulated, leading to the formation of more solid plasma gratings. Diverse variations are under study to have a firm compression process. The plasma-based optics and photonics may pave a promising road to extremely high-power laser technology as shown in Fig. 24.

8 Future prospects

In this paper, the laser plasma physics research and applications in Korea were reviewed. Although the laser plasma research activities have a rather short history compared with other types of plasma research, remarkable progress has been achieved in basic laser plasma physics research and applications. The progress includes the novel particle acceleration of electrons and protons/ions, THz wave generation, future light source development, high-energy-density plasma physics, plasma optics, medical applications, etc. We expect scientific advances in laser plasma physics to continue with the rapid advances in high-power laser technologies and more scientific achievements to be utilized for industrial and medical applications. Furthermore, some dreams of laser

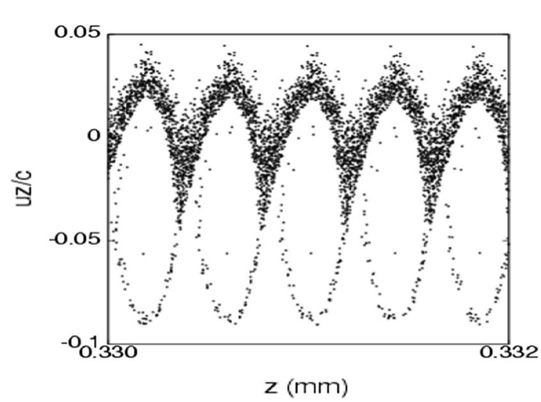

Fig. 24 Trapping of electrons in the plasma wave

plasma physics, for example, LWFA-based X-ray FELs, might be realized in the near future.

Acknowledgements One of the authors (H.S.) would like to give special thanks to Dongho Kim at ETRI for useful discussions related with their activities.

References

1. S. Augst et al., JOSA B **8**, 858 (1991)
2. D. Strickland, G. Mourou, Opt. Commun. **55**, 447 (1985)
3. J.W. Yoon et al., Optica **8**, 630 (2021)
4. N. Hafz et al., Phys. Rev. E **73**, 016405 (2006).
5. I. Nam, Curr. Appl. Phys. **15**, 468 (2015)
6. T.J. Yu et al., Opt. Express **20**, 10807 (2012)
7. J.H. Sung et al., Opt. lett. **42**, 2058 (2017)
8. S.K. Lee, H.T. Kim, I.W. Choi, C.M. Kim, C.H. Nam, J. Korean Phys. Soc. **73**, 179 (2018)
9. E. Esarey, P. Sprangle, J. Krall, A. Ting, IEEE Trans. Plasma Sci. **24**, 252 (1996)
10. D. Umstadter, Phys. Plasmas **8**, 1774 (2001)
11. T. Tajima, J.M. Dawson, Phys. Rev. Lett. **43**, 267 (1979)
12. S.C. Wilks et al., Phys. Plasmas **8**, 542 (2001)
13. B. Qiao et al., Phys. Rev. Lett. **105**, 155002 (2010)
14. C. D'Amico et al., Phys. Rev. Lett. **98**, 235002 (2007)
15. V.M. Malkin, G. Shvets, N.J. Fisch, Phys. Rev. Lett. **82**, 4448 (1999)
16. S. Kneip et al., Nat. Phys. **6**, 980 (2010)
17. M.S. Kim et al., Appl. Phys. Lett. **102**, 204103 (2013)
18. J. Kim et al., Rev. Sci. Instrum. **92**, 023511 (2021)
19. T.D. Arber et al., Plasma Phys. Control. Fusion **57**, 113001 (2015)
20. I. Nam, Ph.D Thesis, GIST (2015).
21. A. Modena et al., IEEE Trans. Plasma Sci. **24**, 289 (1996)
22. C. DesRosiers, V. Moskvin, A.F. Bielajew, L. Papiez, Phys. Med. Biol. **45**, 1781 (2000)
23. V. Malka, J. Faure, Y.A. Gaudeul, Mutat. Res. **704**, 142 (2010)
24. B. Palma et al., Radiother. Oncol. **119**, 154 (2016)
25. A. Subiel et al., Phys. Med. Biol. **59**, 5811 (2014)
26. T. Fuchs et al., Phys. Med. Biol. **54**, 3315 (2009)
27. A. Subiel et al., Phys. Med. **42**, 327 (2017)
28. J. Kim, Y.H. Hwangbo, K.N. Kim, Plasma Phys. Control. Fusion **60**, 034008 (2018)
29. J. Kim, Y. Hwangbo, W.-J. Ryu, K.N. Kim, S.H. Park, J. Instrum. **11**, C03012 (2016)
30. J. Jo et al., in Proceeding of FEL2015, 739 (Daejeon, Korea, 2015).
31. S. H. Park et al., in Proceedings of SPIE - The International Society for Optical Engineering **8075**, 33 (Prague, Czech Republic, 2011).
32. S. H. Park et al., 6th International Particle Accelerator Conference, 2569 (2015).
33. W. Wang et al., Nature **595**, 516 (2021)
34. C.A. Lindstrøm et al., Phys. Rev. Lett. **121**, 194801 (2018)
35. C. Joshi, V. Malka, New J. Phys. **12**, 045003 (2010)
36. ALEGRO collaboration, arXiv: 1901. 10370 v2 (2019).
37. AWAKE collaboration, Nature **561**, 363 (2018).
38. Seong-Yeol Kim, Ph.D Thesis, UNIST (2021).
39. S. Y. Kim et al., Nucl. Instrum. Methods Phys. Res. Section A **953**, 163194 (2020).
40. S.Y. Kim et al., Phys. Rev. Accel. Beams **24**, 021301 (2021)
41. K. J. Moon et al., 47th EPS Conference on Plasma Physics (2021).
42. K.-J. Moon et al., Phys. Plasmas **26**, 073103 (2019)
43. Jimin Seok et al., in Proceedings of 18th Advanced Accelerator Concepts Workshop (2018).
44. Seong-Yeol Kim et al., arXiv: 2104. 10288 (2021).
45. R.A. Snavely et al., Phys. Rev. Lett. **85**, 2945 (2000)
46. W. Ken, D. Ledingham et al., Appl. Sci. **4**, 402 (2014)
47. J.C. Fernandez et al., Nucl. Fusion **54**, 054006 (2014)
48. V. Malka et al., Med. Phys. **31**, 1587 (2004)
49. A. Macchi, A Superintense Laser-Plasma Interaction Theory Primer, Springer (2013).
50. L.O. Silva et al., Phys. Rev. Lett. **92**, 015002 (2004)
51. K. Lee et al., Phys. Rev. E **78**, 056403 (2008)
52. K. Lee et al., Phys. Plasmas **18**, 013101 (2011)
53. I.J. Kim et al., Phys. Plasmas **23**, 070701 (2016)
54. A. Higginson et al., Nat. Commun. **9**, 724 (2018)
55. H. Schwoerer et al., Nature **439**, 445 (2006)
56. B.M. Hegelich et al., Nature **439**, 441 (2006)
57. S. Ter-Avetisyan et al., Phys. Rev. Lett. **93**, 155006 (2004)
58. D. Haberberger et al., Nat. Phys. **8**, 95 (2012)
59. P. Hilz et al., Nat. Comm. **9**, 423 (2018)
60. K.N. Kim et al., Phys. Plasmas **21**, 043110 (2014)
61. K.N. Kim et al., Phys. Plasmas **23**, 033119 (2016)
62. M. Kumar et al., AIP Adv **9**, 045304 (2019)
63. National Research Council, Frontiers in High Energy Density Physics: The X-Games of Contemporary Science (Washington, DC, USA, 2003), pp. 1-176
64. B.I. Cho, Appl. Sci. **9**, 4812 (2019)
65. Daligault and S. Gupta, Astrophys. J. **703**, 994 (2009).
66. S.H. Glenzer et al., Science **327**, 1228 (2010)
67. R.R. Gattass, E. Mazur, Nat. Photonics **2**, 219 (2008)
68. A. Vogel et al., Appl. Phys. B **81**, 1015 (2005)
69. R.W. Lee et al., Laser Part. Beams **20**, 527 (2002)
70. G. Kang and B. I. Cho, Curr. Appl. Phys. in press (https://doi.org/10.1016/j.cap.2021.05.006).
71. C. Bostedt et al., Rev. Mod. Phys. **88**, 015007 (2016)
72. J.W. Lee et al., Nuclear Inst. Methods Phys. Res. A **895**, 120–125 (2018)
73. G. Kang et al., Nuclear Inst. Methods Phys. Res. A **922**, 114–118 (2019)
74. J.W. Lee et al., J. Synchrotron Radiat. **27**, 953–958 (2020)
75. B.I. Cho et al., PRL **106**, 167601 (2011)
76. K. Engelhorn et al., PRB **91**, 214305 (2015)
77. B.I. Cho et al., Sci. Rep. **6**, 18843 (2016)
78. A. Fernandez-Pañella et al., PRB **101**, 184309 (2020)
79. S.M. Vinko et al., Nature **482**, 59 (2012)
80. B.I. Cho et al., PRL **109**, 245003 (2012)
81. D.S. Rackstraw et al., PRL **114**, 015003 (2015)
82. B.I. Cho et al., PRL **119**, 075002 (2017)
83. H.-K. Chung et al., AIP Conference Proceedings 1811, 020001 (2017)
84. M.S. Cho et al., Phys. Plasmas **25**, 053301 (2018)
85. W. Bang et al., Phys. Rev. E **88**, 033108 (2013)
86. W. Bang et al., Phys. Plasmas **20**, 093104 (2013)
87. T. Ditmire et al., Nature **398**, 489 (1999)
88. J. Zweiback et al., Phys. Rev. Lett. **84**, 2634 (2000)
89. W. Bang et al., Phys. Rev. E **87**, 023106 (2013)
90. W. Bang, Phys. Rev. E **92**, 013102 (2015)
91. W. Bang et al., Phys. Rev. Lett. **111**, 055002 (2013)
92. M. Barbui et al., Phys. Rev. Lett. **111**, 082502 (2013)
93. H. Hamster, A. Sullivan, S. Gordon, W. White, R.W. Falcone, Phys. Rev. Lett. **71**, 2725 (1993)
94. K.Y. Kim, A.J. Taylor, J.H. Glownia, G. Rodriguez, Nat. Photonics **2**, 605 (2008)
95. K. Kang, S. Lee, D. Jang, J. Kim, H. Suk, Plasma Phys. Control. Fusion **62**, 125008 (2020)

96. D. Jang, H.S. Uhm, D. Jang, M.S. Hur, H. Suk, Plasma Sources Sci. and Technol. **25**, 065008 (2016)
97. G. Shvets, N.J. Fisch, A. Pukhov, J. Meyer-ter-Vehn, Phys. Rev. Lett. **81**, 4879 (1998)
98. R.M.G.M. Trines et al., Nat. Phys. **7**, 87 (2011)
99. X. Yang et al., Sci. Rep. **5**, 13333 (2015)
100. G. Vieux et al., Sci. Rep. **7**, 2399 (2017)
101. M.S. Hur, G. Penn, J.S. Wurtele, R. Lindberg, Phys. Plasmas **11**, 5204 (2004)
102. M.S. Hur, R.R. Lindberg, A.E. Charman, J.S. Wurtele, H. Suk, Phys. Rev. Lett. **95**, 115003 (2005)
103. S. Yoffe et al., Phys. Rev. Res. **2**, 013227 (2020)